Counting point defects at nanoparticle surfaces by electron holography

Yan Lu,[*,†,‡] Fengshan Zheng,[*,†] Qianqian Lan,[†] Michael Schnedler,[*,†] Philipp Ebert,[†] and Rafal E. Dunin-Borkowski[†]

†*Ernst Ruska-Centre for Microscopy and Spectroscopy with Electrons (ER-C 1) and Peter Grünberg Institute (PGI 5), Forschungszentrum Jülich GmbH, 52425 Jülich, Germany*

‡*Beijing Key Lab and Institute of Microstructure and Properties of Advanced Materials, Beijing University of Technology, Beijing, 100124, China*

E-mail: y.lu@fz-juelich.de; f.zheng@fz-juelich.de; m.schnedler@fz-juelich.de

Abstract

Metal oxide nanoparticles exhibit outstanding catalytic properties, believed to be related to the presence of oxygen vacancies at the particle's surface. However, little quantitative is known about concentrations of point defects inside and at surfaces of these nanoparticles, due to the challenges in achieving an atomically resolved experimental access. By employing off-axis electron holography, we demonstrate using MgO nanoparticles as an example, a methodology which discriminates between mobile charge induced by electron beam irradiation and immobile charge associated with deep traps induced by point defects as well as distinguish between bulk and surface point defects. Counting the immobile charge provides a quantification of the concentration of F^{2+} centers induced by oxygen vacancies at the MgO nanocube surfaces.

Keywords

MgO nanoparticles; off-axis electron holography; F-centers; point defect quantification

Metal oxide nanoparticles have developed rapidly into materials of choices for a wide field of technologies, spanning from medical to catalytic applications.[1–4] For example, MgO nanoparticles exhibit antibacterial properties,[5] which are believed to originate from oxygen vacancies at the nanoparticle surfaces.[6] MgO nanoparticles also promote a wide variety of catalytic reactions, e.g., allowing a reduction of pollutants,[7–9] as well as splitting or decomposition of molecules.[10,11] The catalytic activity is also supposed to be mediated by surface point defects.[12,13] Hence, quantification of point defect densities at surfaces of metal oxide nanoparticles is vital for understanding the physical and chemical processes at nanoparticle surfaces and for improving current and future applications.

In principle, defects on insulating metal oxide nanoparticle surfaces could be imaged directly by scanning probe microscopy, although extremely challenging due to the small particle size, or probed indirectly through electron paramagnetic resonance spectroscopy (with limitations in distinguishing bulk from surface defects).[10] Transmission electron microscopy (TEM) has been shown to be able to image individual impurities in a matrix material through the difference in Z contrast[14] and to probe the local bulk oxygen vacancy concentration in perovskites.[15] The former approach does, however, not work for small Z differences expected for intrinsic defects at surfaces and the latter lacks sensitivity for surfaces. Hence, a different access to surface point defects of nanoparticles is needed.

Point defects on metal oxide surfaces are mostly deep level centers, with energy levels deep in the band gap, trapping charge carriers and thereby giving rise to surface charge.[10,16] Therefore, an alternative way to quantify the concentration of point defects is to probe their charge. However, probing the charge at the surface of a nanoparticle is a rather delicate task. On the other hand, off-axis electron holography in the TEM can probe the electrostatic potential and thereby the charge of individual nanoparticles and identify the spatial location of the charge.[17,18] Thus far, such charge observed by TEM on metal oxide nanoparticles (and

other insulating materials) is attributed to electron beam charging,[18] and thus is anticipated to be extrinsic.

Here we demonstrate a methodology to distinguish mobile charge induced by electron beam irradiation and charge trapped in deep levels associated with defects, and furthermore discriminate between charged bulk and surface defects. This allows us to extract the intrinsic concentration of surface point defects on individual nanoparticles using off-axis electron holography.

We illustrate the methodology using MgO nanocubes prepared by burning Mg pellets in air and collecting the combustion smoke with a lacey carbon grid. Individual nanocubes were picked up from the grid using a W needle in a Nanofactory scanning tunneling microscopy-TEM holder. These cubes were then characterized by off-axis electron holography in an image-aberration-corrected FEI Titan G^2 60-300 microscope[19] equipped with an electron biprism and operated at 300 kV in the Lorentz mode. Electron holograms of nanocubes with corresponding reference holograms in the adjacent vacuum were acquired using a 4K×4K Gatan K2 direct electron detector using an exposure time of 6 s. The spatial variation of the electron phase $\varphi(x, y)$ induced by the electric field of the nanocubes is then reconstructed using Holoworks (Gatan). For every MgO nanocube investigated, the reconstructed phase images, acquired at different dose rates, were then aligned to ensure that the phase profiles were extracted always at same spatial position.

The electron phase is given in the absence of magnetic fields and dynamical diffraction by[17,20]

$$\varphi(x, y) = C_E \int_{-\infty}^{+\infty} \big(V_{\mathrm{Q}}(x, y, z) + V_{\mathrm{MIP}}(x, y, z)\big) dz, \tag{1}$$

where z is the incident electron beam direction and C_E an interaction constant with a value of 6.53 $\times 10^6$ rad/(V·m) for 300 kV electrons. V_{Q} and V_{MIP} are the electrostatic potential induced by charge and the mean inner potential (MIP) of the MgO nanocube, respectively.

Theoretical phase maps and respective line profiles of MgO nanocubes were calculated based on a numerical integration of the electrostatic potential of a uniformly charged cubic

shell.[21] Furthermore, a constant MIP of 13.01 V and a relative permittivity of 9.5 was assumed for MgO.[22,23] For keeping overall charge neutrality, an oppositely charged cube was set in a distance of 5 μm, i.e. sufficiently far away that the potential in the field of view is not affected.

Figure 1a shows a typical unwrapped phase map of a MgO nanocube acquired by off-axis electron holography at a dose rate of 4.1 $e/\text{Å}^2/\text{s}$. The nanocube is attached to a nano-sized W needle on the upper left side. A $\langle 110 \rangle$ direction of nanocube is oriented almost parallel to the beam direction, yielding a rectangular projected shape, whose edge is shown in greenish-blue color. Within this rectangle, the phase change is much larger than outside in the vacuum. This indicates that the contribution of the MIP inside the MgO cube to the phase integral is significantly larger as compared to the contribution of the electrostatic potential [cf. Eq.(1)]. Since we focus on the charge-induced electrostatic potential of the MgO nanocube, we turn to the phase in the vacuum region around the nanocube, where no inner potential exists. The projected phase contours (iso-phase lines) with spacing of $2\pi/8$ radian, shown in Fig. 1b, illustrate the stray field distribution around the nanocube in the vacuum. The phase shift decreases monotonically in the radial direction. The decay is further quantitatively visualized in Fig. 2 using an exemplary phase profile (gray symbols) acquired along the direction of the arrow in Fig. 1a, i.e the direction where the profile is furthest away from the W tip and close to parallel to the biprism filament (for the choice of direction of the profile see Sect. 2 in Supporting Information). The shape of the phase decay indicates the presence of an electric field attributed to a positively charged MgO nanocube.

In order to corroborate this finding, the measured phase map is compared to a simulated phase map of a nanocube with a uniform positive surface charge density of 3×10^{10} e/cm^2 (below it is shown that no bulk charge is present inside the nanocube). The simulation reproduces the shape and phase shifts within the projected nanocube area very well (compare Fig. 1c and d). In addition, good agreement is also found in the vacuum: Figure 2 compares the measured phase profile with simulated ones for different surface charge densities (colored

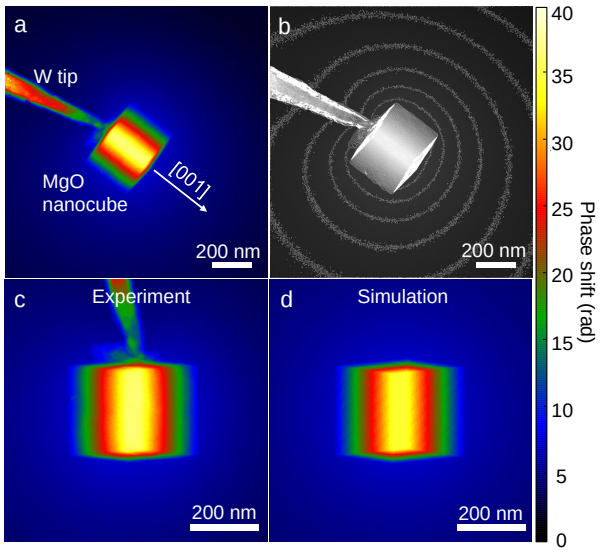

Figure 1: (a) Phase map of a MgO nanocube with a size of 260 nm acquired at a dose rate of 4.1 $e\text{Å}^{-2}\text{s}^{-1}$ and (b) corresponding phase contours with the contour spacing of $2\pi/8$. The electron beam direction is close to the $\langle 110 \rangle$ zone axis. (c, d) Comparison between (c) measured and (d) simulated phase maps of the nanocube, revealing an excellent agreement. The simulation was computed by numerical integration of the electrostatic potential using Eq. (1), assuming a uniform surface charge density of 3×10^{10} e/cm^2.

curves). The best agreement is found for a surface charge density of 3.03×10^{10} e/cm^2 (based on minimization of sum of squared deviations, see inset of Fig. 2).

Next, we estimate the effect of the non-sphericity of the nanocube on the potential. The aim is to assess if the total charge of the cube can be determined with sufficient accuracy by fitting the phase decay on basis of the centrosymmetric Coulomb potential only. Inserting the Coulomb potential of a point charge q (and a compensating charge positioned in infinity, to ensure charge neutrality and convergence) in Eq. (1) and integrating along the beam direction z yields for the phase profile[24]

$$\varphi(x) = -C_\text{E} \cdot \frac{q}{4\pi\epsilon_0} \ln\left(x/x_0\right)^2 + \varphi_0 \tag{2}$$

where x is the distance to the point charge, x_0 the distance unit, and φ_0 the phase background and offset. The red dashed line in Fig. 2 reveals an excellent description of the measured phase decay over very large distances. The obtained charge is $q = (119 \pm 10)$ e, equivalent to

a surface charge density of $(2.86 \pm 0.24) \times 10^{10}$ e/cm^2. This agrees within the error margin with the charge density obtained from the simulation. Hence, the non-sphericity can be neglected. Therefore, for the sake of practicability, from now on we analyse the total charge (bulk and surface) by fitting of the centrosymmetric Eq.(2) to the phase decay in the vacuum, keeping in mind that the deviation of the determined total charge is only in the range of 6%.

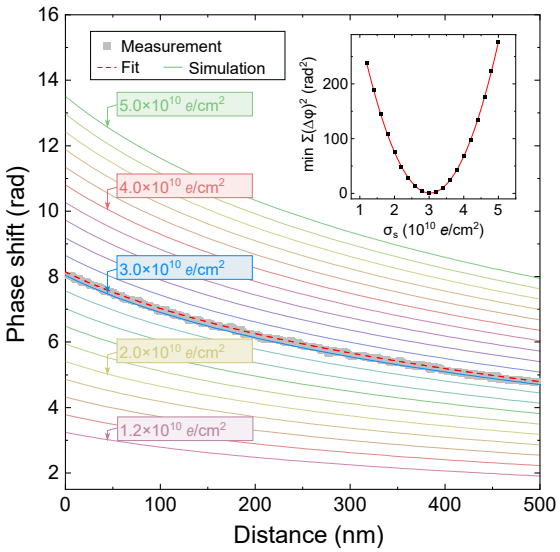

Figure 2: Example of an experimentally measured phase profile (gray symbols) extracted along the [001] direction shown by the arrow in Fig.1a compared to phase profiles obtained from a phase simulation (solid lines) of a nanocube with dimensions of $260 \times 260 \times 270$ nm^3 with different uniform positive surface charge densities (shown in steps of $0.2 \times 10^{10} e/\mathrm{cm}^2$). The dashed red line corresponds to an alternative fit of the experimental phase profile using Eq. 2 based on a centrosymmetric Coulomb potential. Inset: Minimized sum of squared deviations between the experimental phase values and the simulations vs. surface charge density σ_s, revealing the best agreement for $\sigma_\mathrm{s} = 3.03 \times 10^{10} e/\mathrm{cm}^2$.

This analysis is now applied to phase decay in the vacuum acquired at different electron beam dose rates. Figure 3 illustrates examples of measured phase profiles (colored curves) for three different dose rates (increasing and decreasing dose rates, see numbers at left end for the acquisition order). The phase profiles were obtained again in the vacuum region in [001] direction as indicated by the arrow in the sketch shown in the lower left corner of the graph. The best fits using Eq. (2) are shown by gray smooth curves. The slope of the phase profiles is found to increase with the dose rate, indicating that the total charge of the cube is increasing with the dose rate (see analogy in Fig. 2). Furthermore, if the dose rate is lowered

again, the slope decreases. In fact, the phase profiles measured at the same dose rate are very similar and independent of the dose rate history (compare phase profiles 1 and 5 or 2 and 4 in Fig. 3, respectively). This is corroborated by the inset of Fig. 3 displaying the total charge (extracted from the gray fits using Eq. (2)) vs. dose rate. The data reveal (i) a full reversibility (compare red and blue symbols, corresponding to the extracted charge during increasing and decreasing dose rate, respectively) and (ii) a linear dependence on the dose rate, but with a large offset of $q_0 = \left(96^{+35}_{-5(\mathrm{sys})} \pm 3.245_{(\mathrm{stat})}\right)\ e$, obtained using a linear fit (see Sect. 2 in the Supporting Information for handling of errors and fitting procedures). This suggests that two different charging mechanisms are present: One is dose rate dependent and reversible, whereas the other one is dose rate independent and non-reversible.

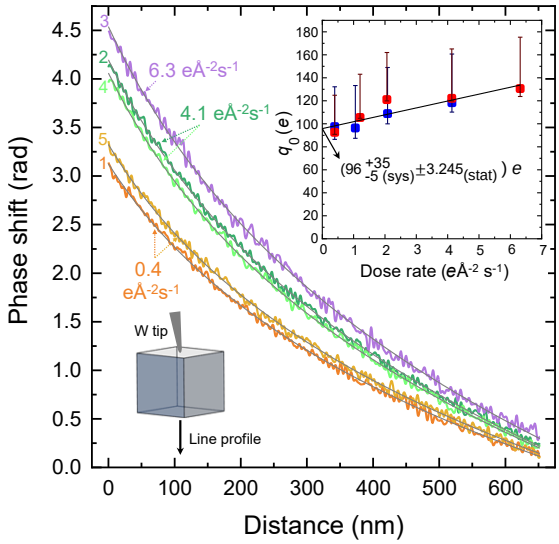

Figure 3: Phase profiles (colored curves) as a function of the distance from the 260 nm-sized cube along the [001] direction acquired at various electron beam dose rates as indicated. Gray solid lines are fits using Eq. (2). The numbers at left end of the curves indicate the acquisition order. The upper right inset displays the surface charge derived from the phase profiles as a function of the dose rate and a linear fit as solid black line. Red (blue) symbols show the charge values obtained during increasing (decreasing) dose rate. The charge exhibits a reversible linear relationship vs. dose rate, with a large offset (intercept with zero electron beam dose rate) of $q_0 = \left(96^{+35}_{-5(\mathrm{sys})} \pm 3.245_{(\mathrm{stat})}\right)\ e$.

Next, we address the spatial location of the charge within the MgO nanocubes. For this purpose, the charge of various MgO nanocubes with different sizes were investigated as

described above. Figure 4 shows the dose-rate independent charge q_0 obtained by extrapolation to zero electron beam dose rate (filled blue symbols) as a function of the cube size. In addition, the charge probed at an unreported dose rate of a prior work[18] is shown as open symbols for comparison. The data reveal a strong increase of the charge with the nanocube size.

Charge could be present in the bulk and on the surfaces of the nanocube. The q_0 is then given for an ideal cube with edge length a by $q_0 = 6a^2\sigma_\mathrm{s} + a^3\sigma_\mathrm{v}$, where σ_s and σ_v are the surface and bulk charge densities, respectively. The best fit of the filled blue diamonds in Fig. 4 (red line) yields a surface charge density of $\sigma_\mathrm{s} = \left(6.7^{+0.9}_{-1.3(\mathrm{sys})} \pm 2.9_{(\mathrm{stat})}\right) \times 10^{10}\ e/\mathrm{cm}^2$ and a bulk charge density of $\sigma_\mathrm{v} = \left(-3.4^{+16.6}_{0(\mathrm{sys})} \pm 51.3_{(\mathrm{stat})}\right) \times 10^{14}\ e/\mathrm{cm}^3$. Considering the error bars and the deduced magnitudes of surface / bulk charge densities, one can conclude that the charge is located on the surfaces of the MgO nanocubes only and the bulk charge is below the detection limit (see also Sect. 2 in Supporting Information for significance of fit model). This result is also corroborated by a prior electron holography study of very small cubes.[18]

At this stage, we would like to add a brief discussion of the precision of the presented charge measurements here by off-axis electron holography. The shape of the iso-phase lines in Fig. 1b reveals that the electrostatic potential in the vacuum is not fully centrosymmetric. On the one hand, the W needle alters the potential locally in its vicinity. Therefore, we focus on the phase profiles furthest away from the needle. On the other hand, the reference beam, used for interference with the part of the beam passing through the sample, is also affected by the extended tail of the Coulomb potential surrounding the MgO nanocube.

This effect cannot be compensated by the subtraction of a so-called reference hologram, which maps the background phase distribution of the microscope itself, since it is experimentally acquired without presence of sample/tip and thus without charge. Therefore, objects with widely extending stray fields, lead to an asymmetry in the phase map primarily perpendicular to the direction of the biprism filament used for interference.[24,25] In Fig. 1b,

the biprism filament is roughly parallel to the [001] direction. In view of this situation, we estimate the upper and lower limits of the charge by analyzing phase profiles extracted perpendicular to the biprism filament in both directions (for further details see Sect. 2 in Supporting Information). The thereby obtained charge values were used as systematic errors and as upper and lower error bars in Figs. 3 as well as 4.

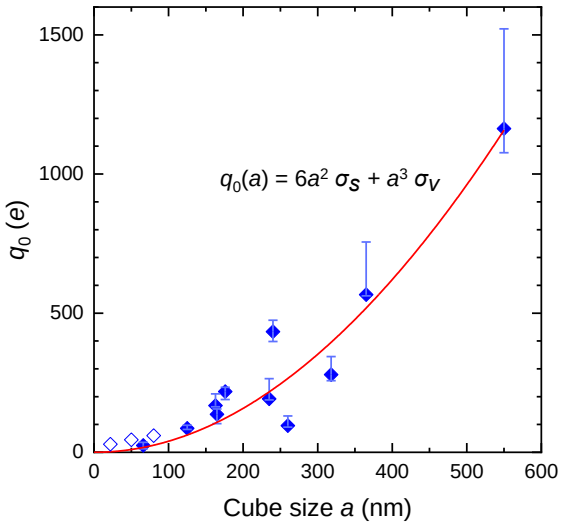

Figure 4: Charge vs. size of the MgO nanocubes. The solid symbols represent the extrapolated charge corresponding to zero electron beam dose rate (see inset in Fig. 3). The error bars of the individual data points reflects the non-sphericity of the vacuum potential (see text for details). The open symbols, derived from the data given in Ref.[18] and probed at an unreported electron dose rate, are for comparison only. The solid red line is the best fit to our experimental data at zero electron beam dose rate. The parabolic term dominates, suggesting that the charge is mostly localized on the surfaces of the nanocubes.

We now address the origin of the MgO nanocubes' surface charge. For this, we recall that we have observed both a reversible (dose rate dependent) charge and non-reversible (zero dose rate) charge. The reversible charging points to the presence of mobile charge carriers (i.e. holes in this case). Thus, a steady state is observed, which is governed by the electron beam induced hole generation (by secondary electron emission) and hole dissipation towards the metallic tip. In contrast, the non-reversible charging points to the presence of completely immobile positive charge carriers, despite contact to the metallic tip. Hence, these immobile charge carriers must be connected to deep traps associated with structural features, which

are immobile at room temperature, such as intrinsic defects or adatoms.

During combustion of the Mg pellets, the freshly-formed MgO nanocubes are in contact with air, i.e. primarily O_2, N_2, H_2O, and CO. In addition, one could conceive that hydrocarbons, e.g. CH_4, C_2H_6, are present on the surfaces of the sample holder and migrate to the MgO. However, these molecules and gases have very low adsorption energies on MgO below 0.5 eV[26,27] and hence desorb well below room temperature in vacuum.[28,29] Furthermore we cleaned all materials of the sample holder before inserting the grid with the MgO nanocubes (see Sect. 1 in Supporting Information for experimental procedures used to assure best cleanliness). Hence, the surface can be considered to be free of adsorbates and thus only intrinsic defects with deep traps can be responsible for the non-reversible charging.

Cathodoluminescence measurements of MgO nanocubes obtained by combustion of Mg in dry air (as used here) reveal only F center related bands, but no other defect or adsorbate bands.[30] Hence, among the many different types of possible intrinsic point defects, the oxygen vacancy related F centers are considered to be the dominant defect for the growth conditions used here. Other intrinsic point defects like the Mg vacancy or more complex di-vacancies require additional gases like H_2 and O_2 as well as irradiation during or after combustion.[30,31]

Furthermore, with a formation energy being lower at the surface than in bulk[32] as well as with a diffusion constant and an activation energy of $3.63\times10^{10}\,\mu\mathrm{m}^2\mathrm{s}^{-1}$ and 3.08 eV,[33] respectively, oxygen vacancies in MgO are able to diffuse from the bulk towards the surface during combustion.[34] Therefore, the oxygen vacancies are primarily located at the surfaces of the MgO nanocubes, in agreement with the dominant location of the positive charge at the surfaces.

At this stage, we turn to the origin of the charging of intrinsic defects. Directly after formation of the MgO nanocubes by combustion, the nanocubes were found to be positively and negatively charged with equal fraction.[35] In contrast, all nanocubes investigated here and previously[18] by TEM exhibit only positive charge. This can be rationalized by considering that the electron beam induces secondary electron emission, leaving holes behind. These

holes get trapped at the defect sites[10] and are immobilized. This process takes place until all defects are positively charged. Note, due to the insulating properties of MgO, there are not enough free electrons in the conduction band to refill the deep trap states in the band gap. In case of oxygen vacancies on MgO(001) surfaces, two electrons can be ultimately removed from the electron states of the neutral vacancy located 2-3 eV above the valence band maximum,[10] yielding a so-called F^{2+} center.

After all F-centers have been positively charged, i.e. all defect states in the band gap are unoccupied, the further generated holes can diffuse freely in the valence band (band structure like in semiconductors[36]), since no hole traps are left. Thereby the holes can reach the MgO-W tip contact. This interface consists of a W-WO_x-MgO junction, where the WO_x layer is approximately 2 nm thick and acts as a tunneling barrier for the holes. Based on W, WO_3, and MgO band gap, Fermi level positions,[36–38] and work functions one can anticipate the transmission coefficient and the resulting tunnel current, to be in the same order as the secondary electron emission current. Hence, an equilibrium between beam-induced hole generation and an outflow of holes through the W-tip is reached.

Note, in principle, the electron beam itself can create F^{2+} centers as well, by ejecting oxygen atoms. However, at the used electron beam energy of 300 keV and dose rate of 4.1 $e/(Å^2 s)$ (i.e. beam current densitiy of 66 A/m^2), this effect is negligible and thus most oxygen vacancies must be present before electron irradiation in the TEM, because of higher voltages (with low current densities) or 4 orders of magnitude higher current densities (with lower voltages) needed to achieve structural damage as reported previously.[39–42] We rather anticipate that the oxygen surface vacancies are formed by desorption under the high temperature conditions present during combustion of Mg. Thus, although the defects are intrinsically present before TEM investigation, electron irradiation is responsible for the charging of the intrinsically present oxygen surface vacancies. This corresponds hence to the non-reversible charging observed experimentally above.

On this basis, the experimentally measured surface charge averaged for all nanocubes of

$\left(6.7^{+0.9}_{-1.3(\mathrm{sys})} \pm 2.9_{(\mathrm{stat})}\right) \times 10^{10}$ e/cm^2 yields a F^{2+} center density at the surface of $\left(3.35^{+0.45}_{-0.65(\mathrm{sys})} \pm 1.45_{(\mathrm{stat})}\right) \times 10^{10}$ cm^{-2} detected by off-axis electron holography. Note, independent of the dominating defect type, the measurement of *immobile* charge carriers in deep traps provides a direct access to the defect concentration (divided by the charge state).

In summary, we have measured the intrinsic concentration of surface point defects on MgO nanocubes, formed by dry combustion of Mg, using off-axis electron holography to $\left(3.35^{+0.45}_{-0.65(\mathrm{sys})} \pm 1.45_{(\mathrm{stat})}\right) \times 10^{10}$ cm^{-2}. The quantification of point defects is based on the distinction of mobile charge carriers, induced by electron beam irradiation, from immobile charge carriers associated with deep traps induced by oxygen surface vacancies as well as the ability to distinguish between surface and bulk charge. The ability of counting point defects through charge measurements can be anticipated to open the path toward the quantification of reaction sites for a wide range of metal oxide nanoparticles.

Supporting Information Available

Details on sample preparations and experimental procedures; sources and estimation of systematic errors; propagation of errors and significance of fit models; analysis of impurities in the Mg pellets before combustion. The Supporting Information is available free of charge via the internet at https://pubs.acs.org.

Acknowledgement

The authors thank M. Farle and coworkers (Univ. Duisburg-Essen), V. Migunov, W. Pieper, and R. Speen for technical help and P. Paciok, M. Faley and L. Kibkalo for support during preparation of MgO cubes. Y.L. thanks for the funding from the Office of China Postdoc Council (OCPC) and the Helmholtz Association. F. Z. and R. D.-B acknowledge the European Union for funding through the Marie Curie Initial Training Network SIMDALEE2 (Grant No. 606988 under FP7-PEOPLE-2013-ITN). R. D.-B. thanks the Deutsche

Forschungsgemeinschaft for a Deutsch-Israelische Projektkooperation (DIP) Grant and the European Union's Horizon 2020 Research and Innovation Programme Q-SORT (Grant No. 766970 under H2020-FETOPEN-2016-2017).

References

(1) Di, D.-R.; He, Z.-Z.; Sun, Z.-Q.; Liu, J. A new nano-cryosurgical modality for tumor treatment using biodegradable MgO nanoparticles. Nanomed. Nanotechnol. **2012**, 8, 1233 – 1241.

(2) Wang, A.; Li, J.; Zhang, T. Heterogeneous single-atom catalysis. Nat. Rev. Chem. **2018**, 2, 65–81.

(3) Beniya, A.; Higashi, S. Towards dense single-atom catalysts for future automotive applications. Nat. Catal. **2019**, 2, 590–602.

(4) Song, Y.; Ozdemir, E.; Ramesh, S.; Adishev, A.; Subramanian, S.; Harale, A.; Albuali, M.; Fadhel, B. A.; Jamal, A.; Moon, D., et al. Dry reforming of methane by stable Ni–Mo nanocatalysts on single-crystalline MgO. Science **2020**, 367, 777–781.

(5) Tang, Z.-X.; Lv, B.-F. MgO nanoparticles as antibacterial agent: preparation and activity. Braz. J. Chem. Eng. **2014**, 31, 591 – 601.

(6) Krishnamoorthy, K.; Manivannan, G.; Kim, S. J.; Jeyasubramanian, K.; Premanathan, M. Antibacterial activity of MgO nanoparticles based on lipid peroxidation by oxygen vacancy. J. Nanoparticle Res. **2012**, 14, 1063.

(7) Davini, P.; Tartarelli, R. Emissions from the combustion of heavy oils: Effect of granulometry and surface area of MgO additive. Fuel **1985**, 64, 380 – 383.

(8) Mahdavi, S.; Jalali, M.; Afkhami, A. Heavy metals removal from aqueous solutions

using TiO_2, MgO, and Al_2O_3 nanoparticles. Chem. Eng. Commun. **2013**, 200, 448–470.

(9) Moussavi, G.; Mahmoudi, M. Removal of azo and anthraquinone reactive dyes from industrial wastewaters using MgO nanoparticles. J. Hazard. Mater. **2009**, 168, 806 – 812.

(10) Pacchioni, G.; Freund, H. Electron Transfer at Oxide Surfaces. The MgO Paradigm: from Defects to Ultrathin Films. Chem. Rev. **2013**, 113, 4035–4072.

(11) Duan, G.; Yang, X.; Chen, J.; Huang, G.; Lu, L.; Wang, X. The catalytic effect of nanosized MgO on the decomposition of ammonium perchlorate. Powder Technol. **2007**, 172, 27 – 29.

(12) Wu, M. C.; Truong, C. M.; Coulter, K.; Goodman, D. W. Role of F centers in the oxidative coupling of methane to ethane over lithium-promoted magnesium oxide catalysts. J. Am. Chem. Soc. **1992**, 114, 7565–7567.

(13) Yan, Z.; Chinta, S.; Mohamed, A. A.; Fackler, J. P.; Goodman, D. W. The role of F-centers in catalysis by Au supported on MgO. J. Am. Chem. Soc. **2005**, 127, 1604–1605.

(14) Voyles, P. M.; Muller, D. A.; Grazul, J. L.; Citrin, P. H.; Gossmann, H.-J. L. Atomic-scale imaging of individual dopant atoms and clusters in highly n-type bulk Si. Nature **2002**, 416, 826.

(15) Jia, C. L.; Urban, K. Atomic-Resolution Measurement of Oxygen Concentration in Oxide Materials. Science **2004**, 303, 2001–2004.

(16) Richter, N. A.; Sicolo, S.; Levchenko, S. V.; Sauer, J.; Scheffler, M. Concentration of Vacancies at Metal-Oxide Surfaces: Case Study of MgO(100). Phys. Rev. Lett. **2013**, 111, 045502.

(17) Lichte, H.; Lehmann, M. Electron holography-basics and applications. Rep. Prog. Phys. **2007**, 71, 016102.

(18) Gatel, C.; Lubk, A.; Pozzi, G.; Snoeck, E.; Hÿtch, M. Counting elementary charges on nanoparticles by electron holography. Phys. Rev. Lett. **2013**, 111, 025501.

(19) Ernst Ruska-Centre for Microscopy and Spectroscopy with Electrons (ER-C), FEI Titan G2 60-300 HOLO. Journal of large-scale research facilities **2016**, 2, A44.

(20) Dunin-Borkowski, R. E.; Kovács, A.; Kasama, T.; McCartney, M. R.; Smith, D. J. In Springer Handbook of Microscopy; Hawkes, P. W., Spence, J. C. H., Eds.; Springer Handbook; Springer, Cham, 2019; Chapter 16. Electron Holography, pp 767–818.

(21) McCreery, K.; Greenside, H. The electric field of a uniformly charged cubic shell. Am. J. Phys. **2018**, 86, 36–44.

(22) Gajdardziska-Josifovska, M.; McCartney, M.; de Ruijter, W.; Smith, D. J.; Weiss, J.; Zuo, J. Accurate measurements of mean inner potential of crystal wedges using digital electron holograms. Ultramicroscopy **1993**, 50, 285 – 299.

(23) Gao, C.; Wei, T.; Duewer, F.; Lu, Y.; Xiang, X.-D. High spatial resolution quantitative microwave impedance microscopy by a scanning tip microwave near-field microscope. Appl. Phys. Lett. **1997**, 71, 1872–1874.

(24) Zheng, F.; Caron, J.; Migunov, V.; Beleggia, M.; Pozzi, G.; Dunin-Borkowski, R. E. Measurement of charge density in nanoscale materials using off-axis electron holography. J. Electron. Spectrosc. Relat. Phenom. **2020**, 241, 146881.

(25) Matteucci, G.; Missiroli, G.; Nichelatti, E.; Migliori, A.; Vanzi, M.; Pozzi, G. Electron holography of long-range electric and magnetic fields. J. Appl. Phys. **1991**, 69, 1835–1842.

(26) Alessio, M.; Usvyat, D.; Sauer, J. Chemically Accurate Adsorption Energies: CO and H2O on the MgO(001) Surface. J. Chem. Theory Comput. **2019**, 15, 1329–1344.

(27) Alessio, M.; Bischoff, F. A.; Sauer, J. Chemically accurate adsorption energies for methane and ethane monolayers on the MgO(001) surface. Phys. Chem. Chem. Phys. **2018**, 20, 9760–9769.

(28) Oncak, M.; Włodarczyk, R.; Sauer, J. Water on the MgO (001) surface: surface reconstruction and ion solvation. J. Phys. Chem. Lett. **2015**, 6, 2310–2314.

(29) Meixner, D.; Arthur, D.; George, S. Kinetics of desorption, adsorption, and surface diffusion of CO2 on MgO (100). Surf. Sci. **1992**, 261, 141–154.

(30) Pikhitsa, P. V.; Kim, C.; Chae, S.; Shin, S.; Jung, S.; Kitaura, M.; Kimura, S.-i.; Fukui, K.; Choi, M. Two-band luminescence from an intrinsic defect in spherical and terraced MgO nanoparticles. Appl. Phys. Lett. **2015**, 106, 183106.

(31) Chen, Y.; M.Abraham, M. Trapped-hole centers in alkaline-earth oxides. J. Phys. Chem. Solid. **1990**, 51, 747–764.

(32) Scorza, E.; Birkenheuer, U.; Pisani, C. The oxygen vacancy at the surface and in bulk MgO: An embedded-cluster study. J. Chem. Phys. **1997**, 107, 9645–9658.

(33) Ueda, A.; Mu, R.; Tung, Y. S.; Wu, M. H.; Zavalin, A.; Wang, P. W.; Henderson, D. O. Optically measured diffusion constants of oxygen vacancies in MgO. J. Phys.: Condens. Matter **2001**, 13, 5535–5544.

(34) Carrasco, J.; Lopez, N.; Illas, F.; Freund, H.-J. Bulk and surface oxygen vacancy formation and diffusion in single crystals, ultrathin films, and metal grown oxide structures. J. Chem. Phys. **2006**, 125, 074711.

(35) Patterson, H. S.; Whytlaw-Gray, R.; Cawood, W. The structure and electrification of smoke particles. Proc. R. Soc. Lond. A **1929**, 124, 523–532.

(36) Fuchs, F.; Rödl, C.; Schleife, A.; Bechstedt, F. Efficient $\mathcal{O}(N^2)$ approach to solve the Bethe-Salpeter equation for excitonic bound states. Phys. Rev. B **2008**, 78, 085103.

(37) Kleperis, J.; Zubkans, J.; Lusis, A. R. Nature of fundamental absorption edge of WO3. Optical Organic and Semiconductor Inorganic Materials. 1997; pp 186 – 191.

(38) Weinhardt, L.; Blum, M.; Bär, M.; Heske, C.; Cole, B.; Marsen, B.; Miller, E. L. Electronic Surface Level Positions of WO_3 Thin Films for Photoelectrochemical Hydrogen Production. J. Phys. Chem. C **2008**, 112, 3078–3082.

(39) Sibley, W. A. Radiation Damage in Oxides and Other Materials. IEEE Trans. Nucl. Sci. **1971**, 18, 273–280.

(40) Sharp, J.; Rumsby, D. Electron irradiation damage in magnesium oxide. Radiat. Eff. **1973**, 17, 65–68.

(41) Turner, P. S.; Bullough, T. J.; Devenish, R. W.; Maher, D. M.; Humphreys, C. J. Nanometre hole formation in MgO using electron beams. Philos. Mag. Lett. **1990**, 61, 181–193.

(42) Devenish, R. W.; Bullough, T. J.; Turner, P. S.; Humphreys, C. J. Electron-beam machining of MgO and ZnO in the STEM. Inst. Phys. Conf. Ser. No. 89 (EMAG-MICRO 89). 1990; p 215.

Supporting Information

Counting point defects at nanoparticle surfaces by electron holography

Yan Lu [1, 2], Fengshan Zheng [1], Qianqian Lan [1], Michael Schnedler [1], Philipp Ebert [1], and Rafal E. Dunin-Borkowski [1]

1. *Ernst Ruska-Centre for Microscopy and Spectroscopy with Electrons (ER-C 1) and Peter Grünberg Institute (PGI 5), Forschungszentrum Jülich GmbH, 52425 Jülich, Germany*
2. *Beijing Key Lab and Institute of Microstructure and Properties of Advanced Materials, Beijing University of Technology, Beijing, 100124, China*

1. Experimental procedures

A Cu grid covered on one side by lacey carbon is cut into two halves using a razor blade (reinforced scraper blade), cleaned before in ethanol in an ultrasonic bath for 3 min to remove all surface contaminations. Then the combustion smoke of Mg is collected on all surfaces of the half grid and kept in vacuum until insertion into the TEM holder (within less than a day). This minimizes surface contaminations (hydrocarbons, water) of the MgO nanocubes initially clean directly after combustion.

Prior to the TEM experiments the W tip and the sample holder were plasma cleaned to remove any hydrocarbon contaminations. Then the half grid with the MgO nanocube is installed with previously cleaned tweezers and the holder is loaded into the TEM. In the TEM the W tip is then used to pick up MgO nanocube from the previously cut edge of the Cu grid only (see Fig. S1). Hence the MgO nanocubes investigated did not sit on the lacey carbon and only touched the Cu (the others cannot be reached and picked up by the W tip). Hence, all procedures minimize surface contaminations and the MgO nanocubes should have surfaces essentially free of contaminations during the electron holography experiments.

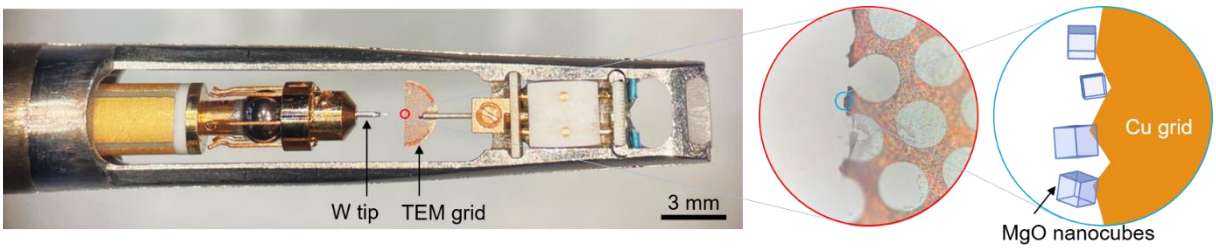

Fig. S1*: NanoFactory STM-TEM holder with W tip to pick up MgO nanocubes sitting on the left side edge of the half Cu grid.*

2. Treatment of errors

A) Sources of systematic errors:
The main sources of systematic errors in the determination of the charge of a nanoparticle is (i) the presence of a W tip used to pick up and manipulate the nanoparticle and (ii) the proximity of a biprism filament used to create a hologram.

(i) The W tip induces a deformation of the centrosymmetric electrostatic potential in its vicinity. This can be well seen in phase maps with isophase lines (Fig. S2). In order to minimize the influence of the

W tip on our results, we extracted the phase profiles in the vacuum (from which the charge is deduced) on the side of the MgO nanocube, which is furthest away from the W tip. The profiles are positioned such that they start from the center of the MgO nanocubes' {100} surface (furthest away from the tip) pointing in normal direction (cf. white arrow in Fig. S2). In this vacuum area the influence of the tip on the potential of the charged MgO nanocube is minimized.

(ii) In addition, the hologram is created by interfering the wave through the nanocube and its vicinity (object wave) with a reference wave passing ideally in a field free region by the nanocube. In reality, the reference wave is still in the region influenced by the Coulomb potential of the charged nanocube and thus in first approximation is affected by a lateral slope in potential. This transfers into an asymmetry in the hologram perpendicular to the biprism filament direction. To minimize the influence of this asymmetry on the measured charge, the tip is positioned roughly parallel to the biprism filament. Thereby the phase change profiles furthest away from the tip, used to deduce the charges, are roughly parallel to the biprism filament, too (Fig. S2). Hence the equi-potential lines in the chosen direction are closest to a centrosymmetric potential compared to any other direction.

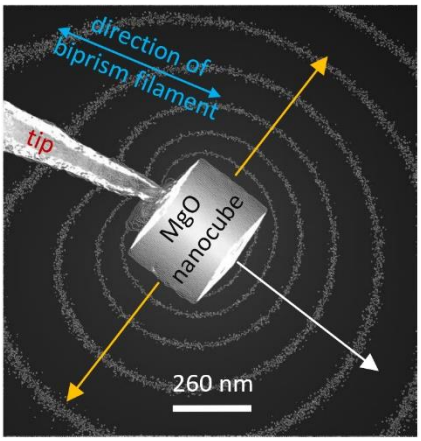

Fig. S2*: Phase map of a MgO nanocube showing phase contours with the contour spacing of 2π/8 (taken from Fig. 1b). The direction of phase change profile used for deducing the charge of the MgO nanocube is indicated by the white arrow. The upper and lower limits of the systematic errors of the charge due to the asymmetry induced by the presence of the biprism and W tip are estimated using perpendicular profiles along the yellow arrows (see text for details).*

B) Estimation of the systematic errors of the charge determination

In order to estimate the effect of the asymmetries induced by the tip and the bisprism on the deduced charge of the MgO nanocubes, we extracted two further line profiles (yellow arrows in Fig. S2) perpendicular to the above mentioned line profile (white arrow in Fig. S2). Along these perpendicular directions, the asymmetric distortion by the biprism is the largest and thus we used the respective profiles for extracting upper and lower limits of the nanocubes' charge.

C) Propagation of errors, fits, and significance of fit models

For the fits shown in Figs. 3 and 4, we treat statistical and systematic errors separately. The systematic errors are due to asymmetries in the phase maps induced by the presence of the W tip and the biprism filament and thus cannot be treated like statistical errors with conventional Gaussian error propagation.

Fit in Fig. 3: Hence, for the fit of the charge vs. electron dose rate data, we performed a chi square minimization without weighting. The *y* intercept of this linear fit provides the immobile charge count.

In order to obtain an upper limit estimate of the systematic error on the charge count, we derived the y-intercepts of linear fits to $y_i+\sigma_{sys,i}^{+}$ and $y_i-\sigma_{sys,i}^{-}$ where $+\sigma_{sys,i}^{+}$ and $-\sigma_{sys,i}^{-}$ are the asymmetric errors in + and $-y$ direction, respectively. This treatment essentially transfers the average systematic error directly to the derived charge count, without reduction due to the number of measurements (as for statistical errors).

In addition to the systematic error, we use the estimated standard error of the y-intercept, as derived by the chi square minimization algorithm, as statistical error of the charge count.

Fit in Fig. 4: For the by chi-square minimization fit of the charge vs. nanocube size data in Figure 4 we treated the systematic and statistical errors in analogy to the above described procedure: The upper and lower limit of the asymmetric systematic errors on the surface and bulk charge densities are estimated using third order polynomial fits to $y_i+\sigma_{sys,i}^{+}$ and $y_i-\sigma_{sys,i}^{-}$ where $+\sigma_{sys,i}^{+}$ and $-\sigma_{sys,i}^{-}$ are the asymmetric systematic errors in + and $-y$ direction. The statistical errors on the surface and bulk charge densities are again obtained by the estimated standard error, derived by the chi square minimization algorithm. The only difference to the fit is Fig.3 is that the individual charge count data points were weighted by their statistical errors in the chi square fit.

We tested three models: Pure bulk, pure surface, and surface plus bulk charge: A pure *bulk* charge model (cubic dependence) is resulting in a coefficient of determination (R^2) of 0.79, which is lower than that of a pure *surface* charge density model (parabolic dependence) of 0.87. The combined model of bulk and surface charge densities has no obvious improvement on the coefficient of determination that is also 0.87, i.e. negligible relative to a pure surface charge density model. This agrees with the fact that the cubic charge density component is below the detection limit, if the error bar is considered as detection limit. Hence, the dominant feature is a surface charge only.

3. Analysis of impurities in the Mg pellets

The following impurities were detected in the Mg pellets used for combustion. The values are given in weight percentage:

Al	0.0226 ± 0.0016
Ca	0.003 ± 0.0007
Fe	0.0024 ± 0.0014
Mn	0.02604 ± 0.00018
Si	0.07 ± 0.04
Zn	0.0042 ± 0.0006

In order to assess if these impurities are really incorporated during combustion, we recall the melting temperature of 2852°C and boiling temperature of 3600°C of MgO. Both are higher than the respective temperatures of the oxides of all found impurities. In particular, the respective temperatures of Mn, Al, and Si oxides are between 600 and more than 2000°C lower and thus it can be anticipated that the impurities will reevaporate from the MgO nanocube at the MgO crystallization temperature. The other impurities incorporated on Mg sites can be expected to exhibit a valence of +2, thus being isoelectronic and not giving rise to charges.